PHYSICAL REVIEW B **76**, 224112 (2007)

Atomistic simulations of tensile and bending properties of single-crystal bcc iron nanobeams

Pär A. T. Olsson,[1,*] Solveig Melin,[1] and Christer Persson[2]
[1]*Division of Mechanics, Lund University, P.O. Box 118, SE-221 00 Lund, Sweden*
[2]*Division of Material Science, Lund University, P.O. Box 118, SE-221 00 Lund, Sweden*

(Received 7 May 2007; revised manuscript received 15 August 2007; published 28 December 2007)

In this paper, we report the results of a systematic study of the elastic properties of nanosized single-crystal wires and beams of bcc iron. Both tensile and bending stiffnesses have been determined employing molecular statics simulations for specimens of different sizes and three different crystallographic orientations. We also analyze the influence of circular cross sections and rounded edges compared to square cross sections with sharp edges for one of the crystallographic orientations. The simulations show that there is a size dependence in Young's modulus and that different crystallographic orientations display different elastic behaviors. There are bands of deviating Young's modulus over the cross sections in the direction 45° from the surfaces emanating from the edges, giving the cross section a heterogeneous character. Rounding the edges, or making the cross section circular, has little influence on the average Young's modulus, but it does influence the distribution over the cross section and, consequently, the aforementioned bands.

DOI: 10.1103/PhysRevB.76.224112 PACS number(s): 62.25.+g, 62.20.Dc, 62.20.−x

I. INTRODUCTION

With the introduction, fast development, and increasing use of nanoelectromechanical systems (NEMS), the mechanical properties of nanostructures have become of considerable interest. NEMS are characterized by their small dimensions, spanning from hundreds down to only a few nanometers, resulting in components of extraordinary force sensitivity, very low mass, high attainable eigenfrequencies, and, sometimes, intriguing magnetic properties. This allows NEMS to act as sensors in highly sensitive detectors in applications involving, e.g., molecular interactions and cell adhesion.[1–7] The low density of defects and the high surface to volume ratio provide the structure with mechanical properties that deviate significantly from those of macroscopic single crystals. Hence, macroscopic continuum mechanical generalizations to the nanoscale may no longer be valid.[8–10]

In the literature, a vast number of papers addressing the issue of mechanical properties of nanostructures have been published. Specially designed experiments to obtain the elastic properties involve mainly two types of setups, e.g., bent cantilever beams[8,10–14] and cantilever resonators.[1–4,9,13,15,16] The two methods differ in the sense that the first is static and uses the continuum mechanical relation between the deflection and the applied force of a cantilever beam to obtain Young's modulus. The latter is, on the other hand, dynamic and the elastic properties are conceived by measuring the spectrum of eigenfrequencies and, through continuum mechanical considerations, Young's modulus is calculated. Experiments indicate that, as the dimensions of a structure reach a certain threshold, surface effects are no longer neglectable. Mechanical properties are reported to deviate significantly from bulk properties, and these deviations are material specific. For instance, it has been observed that for chromium,[10] silicon[15] and gallium nitride,[16] there is a decrease in Young's modulus with decreasing size, whereas for polypyrrole,[12–14] silver,[14] and lead,[14] it has been reported that Young's modulus increases with decreasing size.

Alongside the experimental research, a great deal of theoretical investigations of the elastic properties of nanostructures have been performed.[17–19] Using simple linear nearest neighbor interactions, it has been found that, depending on how the height of the structure is measured, the bending stiffness for a two-dimensional (2D) single-crystal strip of discrete particles takes on different values. This effect does, however, vanish as the number of planes goes toward infinity.[17] Similar results has been found for Young's modulus of 2D hexagonal closed-packed structures and three-dimensional face-centered cubic crystals. Furthermore, it has been reported that this height ambiguity can lead to that Young's modulus may both increase and decrease with increasing size.[18,19]

Different numerical techniques have been employed to simulate the elastic and the plastic behaviors of nanostructures. In the literature, there are basically three types of molecular dynamics simulations that are used to monitor the elastic behavior of a nanostructure; structural frequency response simulations,[20] tensile tests,[21–29] and beam bending simulations.[30] In Ref. 20, the mechanical properties for quartz crystal oscillators have been investigated, and it was argued that it is not sufficient to approximate Young's modulus with only surface and bulk atoms, but the edge atoms must also be taken into account. Consequently, when approximating Young's modulus, the cross sections were divided into three parts, bulk, surfaces, and edges, and contributions from each part were regarded so that an approximate fit to a polynomial with coefficients that were weights corresponding to the individual part's area divided by the full area could be found.

Metallic films and nanowires have been investigated by several investigators.[21–30] The elastic properties of copper films and wires have been simulated through molecular statics (MS) simulations using embedded atom method multibody potentials. It has been observed that different orientations display very different behaviors, i.e., some orientations display increasing Young's modulus whereas others display decreasing Young's modulus with increasing size. These findings have been confirmed with *ab initio* simulations from which it has also been found that there is a correlation between the redistribution of the electron density over the sur-

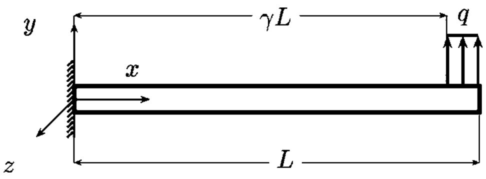

FIG. 1. A cantilever beam clamped at one end.

face layers and the elasticity of the films. However, when using Lennard-Jones pair potentials, all the orientations display monotonous stiffening with increasing size.[26–28] It has also been reported that the size effect gives rise to large tensions in the surfaces, significantly contracting the nanowire length and results in displacements of the surface layers, distorting the local structure from that of the ideal bulk.[22,28,30] In fact, in gold nanowires, there have been observations of surface tensions being sufficiently large to induce a phase transformation.[25]

In this paper, the scaling effects of the bending stiffness and Young's modulus in iron nanobeams and nanowires of body-centered cubic (bcc) crystal structure are addressed employing MS bending and tensile simulations. Iron nanowires can be manufactured through electrodeposition methods,[31] and there has been reports of highly textured iron nanowires having bcc structure[5,6] with diameters well below 20 nm.[5] Three different crystallographic orientations are studied, with the orthogonal (x,y,z) directions in Figs. 1 and 2 corresponding to ([100], [010], [001]), ([110], [001], [$1\bar{1}0$]), and ([110], [$\bar{1}10$], [001]) as illustrated in Figs. 3(a)–3(c). These will subsequently be referred to as orientations I, II, and III, respectively.

II. ELASTIC PROPERTIES OF CUBIC MATERIALS

For general anisotropy, Hooke's generalized law[32] reads

$$\begin{pmatrix} \sigma_{11} \\ \sigma_{22} \\ \sigma_{33} \\ \sigma_{12} \\ \sigma_{13} \\ \sigma_{23} \end{pmatrix} = \begin{pmatrix} C_{11} & C_{12} & C_{13} & C_{14} & C_{15} & C_{16} \\ C_{21} & C_{22} & C_{23} & C_{24} & C_{25} & C_{26} \\ C_{31} & C_{32} & C_{33} & C_{34} & C_{35} & C_{36} \\ C_{41} & C_{42} & C_{43} & C_{44} & C_{45} & C_{46} \\ C_{51} & C_{52} & C_{53} & C_{54} & C_{55} & C_{56} \\ C_{61} & C_{62} & C_{63} & C_{64} & C_{65} & C_{66} \end{pmatrix} \begin{pmatrix} \epsilon_{11} \\ \epsilon_{22} \\ \epsilon_{33} \\ \epsilon_{12} \\ \epsilon_{13} \\ \epsilon_{23} \end{pmatrix}, \tag{1}$$

or, in a more compact notation,

$$\boldsymbol{\sigma} = \mathbf{C}\boldsymbol{\epsilon}, \tag{2}$$

which for cubic symmetry simplifies the stiffness matrix

$$\mathbf{C} = \begin{pmatrix} C_{11} & C_{12} & C_{12} & 0 & 0 & 0 \\ C_{12} & C_{11} & C_{12} & 0 & 0 & 0 \\ C_{12} & C_{12} & C_{11} & 0 & 0 & 0 \\ 0 & 0 & 0 & C_{44} & 0 & 0 \\ 0 & 0 & 0 & 0 & C_{44} & 0 \\ 0 & 0 & 0 & 0 & 0 & C_{44} \end{pmatrix}. \tag{3}$$

For a uniaxial stress state, i.e., when only the normal stress x component σ_{xx} is nonzero, we can define a directional Young's modulus E_{ijk} that satisfies

$$\sigma_{xx} = E_{ijk}\epsilon_{xx}, \tag{4}$$

where the triplet ijk corresponds to the x direction of the cubic cell, i.e., 100 and 110 for orientation I and orientations II and III, respectively. Consequently, the ideal bulk directional Young's modulus for the different orientations may be calculated from[32]

$$\frac{1}{E_{100}} = \frac{C_{11}+C_{12}}{(C_{11}+2C_{12})(C_{11}-C_{12})}, \tag{5}$$

$$\frac{1}{E_{110}} = \frac{C_{11}}{2(C_{11}+2C_{12})(C_{11}-C_{12})} + \frac{1}{8C_{44}}. \tag{6}$$

III. CONTINUUM BEAM THEORY

Bernoulli's beam theory is valid for beams with slender cross sections, i.e., $h/L \ll 1$, where h and L are the height and length, respectively, with small deflections and neglects any shearing of the cross sections, i.e., all the cross sections are assumed to be perpendicular to the centerline of the beam. The differential equation governing Bernoulli's beam theory is written as

$$\frac{d^2}{dx^2}\left(B(x)\frac{d^2w(x)}{dx^2}\right) - K_y(x) = 0, \tag{7}$$

where B is the bending stiffness, K_y is the distributed load per unit length, and w is the deflection in the y direction.[33] With the assumption of constant B along the beam, and with the boundary conditions satisfying

$$w|_{x=0} = 0, \quad \left.\frac{dw}{dx}\right|_{x=0} = 0, \quad \left.\frac{d^2w}{dx^2}\right|_{x=L} = 0, \quad \left.\frac{d^3w}{dx^3}\right|_{x=L} = 0,$$

i.e., clamped end at $x=0$, a free end at $x=L$, and K_y being constant over the portion $(1-\gamma)L$ of the beam, the deflection of the free end, $\delta = w(L)$, for the beam in Fig. 1 can be calculated using superposition to yield

$$\delta = \frac{qL^3}{24B}(3 + 3\gamma + 3\gamma^2 - \gamma^3), \tag{8}$$

where γ denotes the fraction of the total length of the beam that is not loaded and q is the resulting force of the distributed load, i.e., $q = K_y(1-\gamma)L$, cf. Fig. 1. The bending stiffness for an arbitrary cross section is calculated as

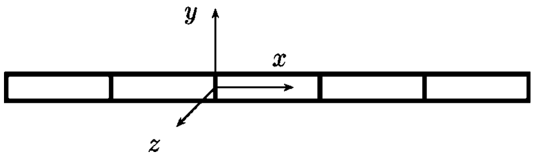

FIG. 2. Nanowire.

$$B = \int_A E_{ijk} y^2 dA, \tag{9}$$

where A denotes the cross-sectional area and y is the y coordinate provided that the origin is chosen so that

$$\int_A E_{ijk} y dA = 0 \tag{10}$$

is satisfied. With a constant E_{ijk} over the cross section Eq. (9) simplifies to

$$B = E_{ijk} \int_A y^2 dA = E_{ijk} I, \tag{11}$$

where I is the moment of inertia.

IV. SIMULATION TECHNIQUE

The cantilever beam under consideration is clamped at one end as schematically illustrated in Fig. 1, where a Cartesian coordinate system with origin at the center of the clamped end is introduced. The clamping condition is effectuated by prescribing zero displacements to the outermost four yz planes of atoms. At the other end of the beam, a load q is distributed on six yz planes of atoms in the y direction over the portion $(1-\gamma)L$ of the beam. In practice, this is achieved by applying external forces, all of equal sizes, in the y direction on all the atoms of the six corresponding planes, adding up to the total external load q. The magnitude of q does vary between the different sizes but is chosen sufficiently small to ensure that small deformations are attained.

The beams are initially relaxed using the so-called fast inertial relaxation engine (FIRE) algorithm, with the parameters $\alpha_S = 0.1$, $N_{min} = 10$, $f_\alpha = 0.99$, $f_{dec} = 0.5$, $f_{inc} = 1.01$, and $\Delta t_{max} = 40\Delta t$, where $\Delta t = 0.509$ fs is the time step.[34] The convergence criterion for relaxation is

$$\sqrt{\sum_{i \neq fixed}^{n} (f_{x,i}^2 + f_{y,i}^2 + f_{z,i}^2)} \leq n 10^{-14} \text{ eV/Å},$$

where n is the total number of atoms and $f_{x,i}$, $f_{y,i}$, and $f_{z,i}$ denote the x, y, and z components of the total force acting on atom i, respectively, i.e., convergence is met when the magnitude of the global force vector of all the nonfixed atoms is sufficiently small. Thereafter, the load q is applied on the beam and the FIRE algorithm is used to find the static deflection, measured as the difference between the y coordinate of the center of mass of the clamped atom planes and the outermost atom plane.

For the nanowire tensile simulations, a somewhat different geometry is adopted. In order to remove any artifacts of finite length, we let the wire consist of an infinite array of identical simulation cells, cf. Fig. 2, i.e., periodic boundary conditions are employed in the x direction. In the periodic direction, 20 yz planes are used for all the simulations in order to ensure that the minimum image convention is not violated.[35] Since all the simulations are performed in the elastic regime, slip bands do not occur and, consequently, no periodic slip bands that may influence the result arise due to the periodic boundary conditions.

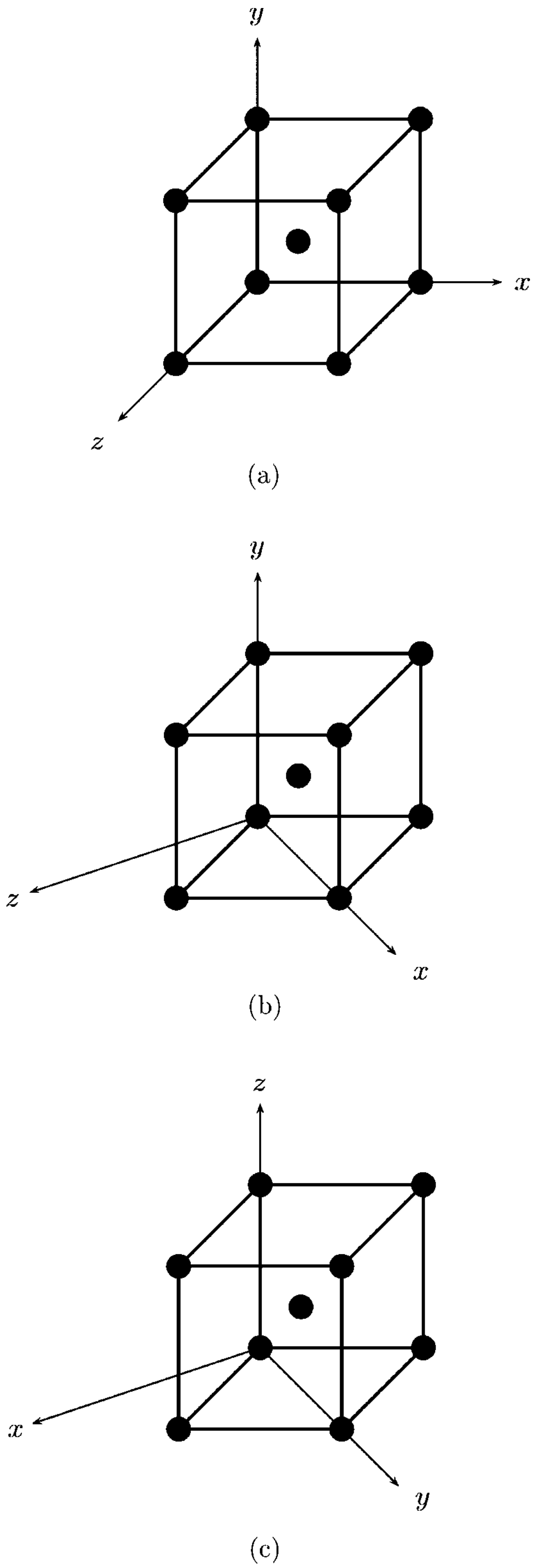

FIG. 3. Coordinate axis orientation for (a) orientation I, (b) orientation II, and (c) orientation III.

Due to the periodic boundary conditions for the nanowire tensile simulations, it is necessary to adopt a two step relaxation procedure for the initial relaxation in order to obtain an

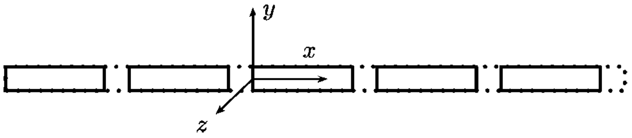

FIG. 4. Deformed nanowire.

initial state where the normal stresses in the x direction are balanced. Therefore, first the average normal pressure in the x direction of the cell is coupled to a Berendsen barostat,[36] which essentially means that the atoms are able to move freely, as the atomic x coordinates are rescaled along with the x dimension of the cell. This results in a state where the x dimension of the cell corresponds to that of a cell where the normal stresses in the x direction are approximately balanced. The cell is also coupled to a heat bath using a Berendsen thermostat.[36] The surrounding pressure and temperature are set to 0 Pa and 0 K, respectively. The time step for the initial relaxation of the nanowires is set to $\Delta t_{ber}=3.563$ fs, and the pressure and temperature coupling times are set to $\tau_p=\tau_T=20\Delta t_{ber}$. In addition to the barostat and the thermostat, kinetic energy is removed using the global convergence algorithm.[37] Secondly, after this relaxation, the FIRE algorithm is employed in order to obtain an equilibrium state. Once this initial, relaxed state of equilibrium is found, the wire is stretched so that the cell and all the atom planes get a uniform strain of 0.1% in the x direction, as schematically illustrated in Fig. 4. From this strained state, a strained state of equilibrium is found using the FIRE algorithm. This means that the atoms in the strained configuration are free to move until they are in a local potential energy minimum while the cell itself remains strained.

In addition to the previously described tensile simulation scheme, we perform tensile simulations of strained nanowires, i.e., only the second part of the initial relaxation scheme is employed. This means that the normal stresses are not necessarily balanced initially and, consequently, the nanowire can be considered to be unrelaxed or prestrained from the state of balanced stresses.

The potential used is of Finnis-Sinclair multibody potential type[38] as modified and given by Machová and Ackland.[39] It has an interaction radius which is extended to $1.3a_0$, where $a_0=2.8665$ Å denotes the lattice constant. This means that the extent of the interaction is between the second and the third closest neighbor. The elastic constants of the interatomic potential are given in Table I,[39] together with the corresponding experimental values.[40] The interatomic forces are calculated using a Verlet neighbor list with a skin thickness of $r_s=1.5$ Å.[35,41,42] This gives every atom an interaction range r_i of $r_i=r_s+1.3a_0=5.226$ Å. The list is updated every 20th time step using a cell-subdivision technique. The time integration is performed using the leapfrog algorithm.[41]

TABLE I. Elastic constants (GPa).

	C_{11}	C_{12}	C_{44}
Potential[a]	243.3	145.0	116.0
Experiment[b]	243.1	138.1	121.9

[a] Reference 39.

[b] Reference 40.

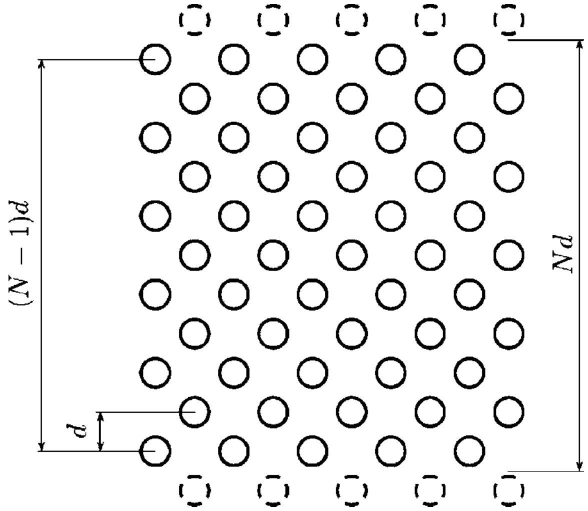

FIG. 5. Height ambiguity (the dashed planes are imaginary atom planes).

When translating continuum beam theory to discrete atomistic calculations, there is an ambiguity when it comes to measuring height, width, and length of the beam.[17–19] From Fig. 5, when considering ordered crystalline structures, it may be natural to regard these quantities as functions of the number of atom planes. Without regarding any surface-relaxation effects, intuitively we should choose, for instance, the height h as a function $h=h(N)$, where N denotes the number of atom planes, expected as $(N-1)d \leq h(N) \leq Nd$, where d denotes the interplanar distance. The effect of N does, however, become neglectable as $N \to \infty$. Identical reasoning leads to analogous results for the width and the length, but considering that the number of planes along the x axis is very large in these simulations, this effect is neglected as regards the length. For simplicity, in this paper, we assume that two adjacent planes equally share the interplanar distance between them.

V. RESULTS AND DISCUSSION

A. Relaxation

During the initial relaxation, atoms tend to displace in order for the stresses to be balanced, meaning that the interplanar distances deviate somewhat from the ideal interplanar distance of a bulk crystal. In Figs. 6(a) and 6(b), the in-plane displacements of two adjacent yz planes, consisting of 15 xy and xz planes, for orientations I and II, respectively, are schematically shown. As can be seen in Fig. 6(a), the edge atoms displace toward the center of the cross section and distort the perfect lattice somewhat. At the centers of the {100} surfaces, the atoms are displaced away from the center, giving the cross section a more rounded character. The same type of surface can be seen at the upper and lower boundaries of the cross section in Fig. 6(b), which is also displaced away from the center of the cross section. Contrary to the {100} surfaces, for the {110} surfaces on the left and the right boundaries,

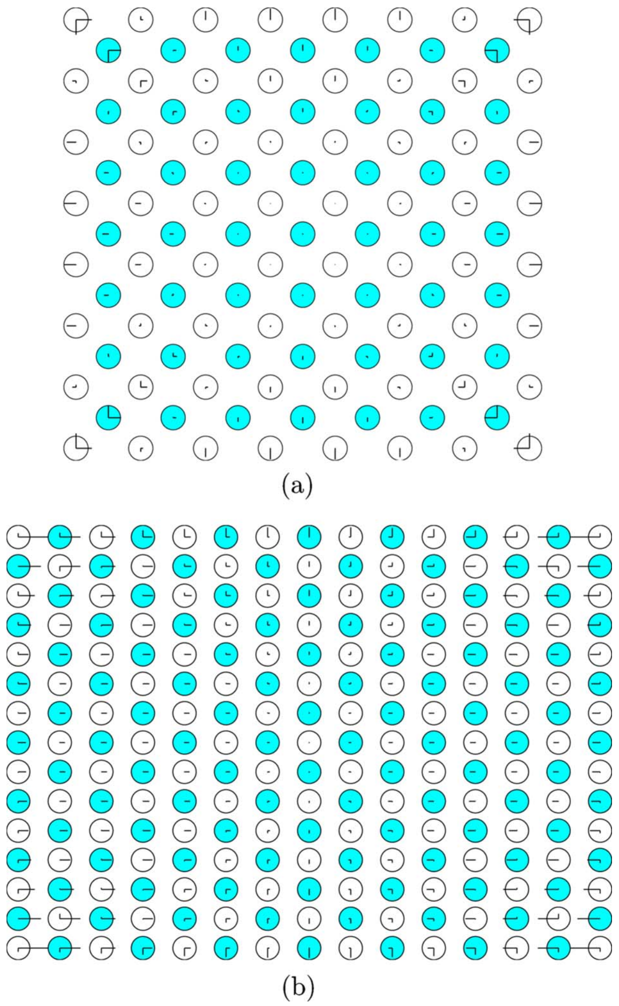

FIG. 6. (Color online) Displacements in the y and z directions for two neighboring yz planes for (a) orientation I and (b) orientation II, where the atoms belonging to different planes have been shaded differently (the magnitudes of the displacements have been multiplied by a factor of 5).

there is an inward displacement. Around the edges for orientation II, the contractions in the $\langle 110\rangle$ directions are the greatest, whereas the displacements in the $\langle 100\rangle$ directions are the smallest, leading to a more rounded cross section.

In order to take these effects into account, the centers of mass for all the yz, xz, and xy planes are measured and the distances between the centers of mass of two adjacent planes are calculated. Then, the average distances, $\langle d_x\rangle$, $\langle d_y\rangle$ and $\langle d_z\rangle$, respectively, over all such pairs are calculated and the three relaxation coefficients λ, κ, and η are defined as

$$\langle d_x\rangle = \lambda d_x, \quad \langle d_y\rangle = \kappa d_y, \quad \langle d_z\rangle = \eta d_z,$$

where d_x, d_y, and d_z denote the ideal interplanar distances between two yz planes, xz planes, and xy planes, respectively, as seen in Table II.

In Figs. 7(a)–7(c), λ, κ, and η can be seen from both the tensile and the bending simulations for all the orientations with cross sections with equally many xy planes as xz planes, i.e., satisfying $N_{xy}=N_{xz}$. For orientation I, cf. Fig. 7(a), it is observed that there is a decrease of λ_{I} with decreasing size, with $\lambda_{\mathrm{I}}=0.953$ for $N_{xy}=N_{xz}=7$ reaching $\lambda_{\mathrm{I}}=0.99$ somewhere in the interval $35 \leqslant N_{xy}=N_{xz} \leqslant 41$, indicating a significant distortion from the perfect bcc lattice. κ_{I} and η_{I} behave dif-

TABLE II. Ideal interplanar distances.

Orientation	d_x	d_y	d_z
I	$a_0/2$	$a_0/2$	$a_0/2$
II	$a_0/\sqrt{2}$	$a_0/2$	$a_0/\sqrt{2}$
III	$a_0/\sqrt{2}$	$a_0/\sqrt{2}$	$a_0/2$

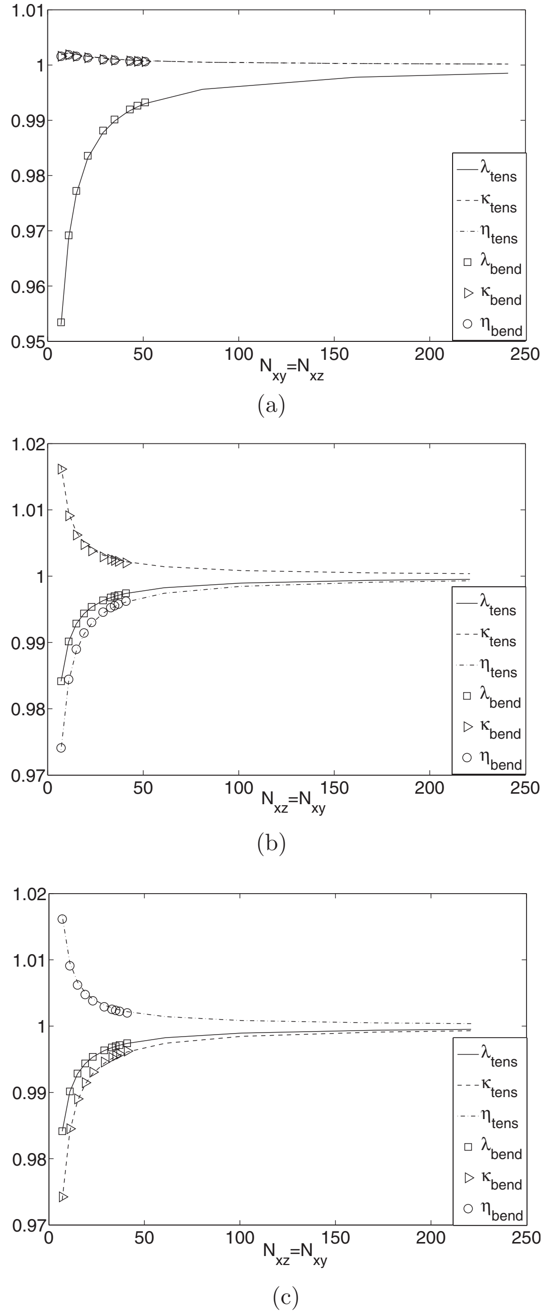

FIG. 7. Relaxation coefficients λ, κ, and η as functions of size for (a) orientation I, (b) orientation II, and (c) orientation III.

ferently in the sense that they increase with decreasing size and reach a maximum for $N_{xy}=N_{xz}=11$, whereafter a decrease is observed between $N_{xy}=N_{xz}=11$ and $N_{xy}=N_{xz}=7$. As expected, due to symmetry, $\kappa_{\mathrm{I}}=\eta_{\mathrm{I}}$ is satisfied and consequently they overlap in Fig. 7(a) and are therefore difficult to distinguish. In Figs. 7(b) and 7(c), the relaxation coefficients of orientations II and III can be seen, respectively. Similar to orientation I, λ_{II} and λ_{III} decrease with decreasing size. However, this decrease is not as significant as for orientation I. Moreover, since orientations II and III are the same except for a 90° rotation around the x axis, we get $\kappa_{\mathrm{II}}=\eta_{\mathrm{III}}$ and $\kappa_{\mathrm{III}}=\eta_{\mathrm{II}}$ as expected, and it is observed that κ_{II} and η_{III} increase with decreasing size, whereas κ_{III} and η_{II} decrease with decreasing size. It can also be noted that there is a slight difference in the relaxation coefficients between those obtained from the tensile simulations and those from the bending simulations, which is believed to be an artifact from the clamping condition.

B. Tensile simulations

In the atomistic simulations, the Cauchy stress tensor can be calculated in the initial and as well as in the final configuration,

$$\boldsymbol{\sigma}=\begin{pmatrix}\sigma_{xx} & \sigma_{xy} & \sigma_{xz}\\ \sigma_{xy} & \sigma_{yy} & \sigma_{yz}\\ \sigma_{xz} & \sigma_{yz} & \sigma_{zz}\end{pmatrix}=-\frac{1}{2V}\sum_{i}^{n}\sum_{j\neq i}\boldsymbol{r}_{ij}\otimes\boldsymbol{f}_{ij}, \tag{12}$$

where V is the volume of the simulation cell, ⊗ the tensor product, and $\boldsymbol{r}_{ij}=\boldsymbol{r}_j-\boldsymbol{r}_i$, where $\boldsymbol{r}_i$ and $\boldsymbol{r}_j$ denote the position vectors of atoms i and j, respectively, and

$$\boldsymbol{f}_{ij}=-\frac{\partial\Phi}{\partial r_{ij}}\frac{\boldsymbol{r}_{ij}}{r_{ij}}, \tag{13}$$

where Φ denotes the potential energy and $r_{ij}=|\mathbf{r}_{ij}|$.[43] Consequently, it is possible to calculate the directional Young's modulus for the simulation cell, E_{ijk}, to be

$$E_{ijk}=\frac{\sigma_{xx}^{f}-\sigma_{xx}^{0}}{\epsilon_{xx}}, \tag{14}$$

where σ_{xx}^{f} and σ_{xx}^{0} denote the average normal stresses for the final and initial configurations, respectively, and ϵ_{xx} denotes the strain of the simulation cell in the x direction, assumed to be

$$\epsilon_{xx}=\frac{l_f-l_0}{l_0}, \tag{15}$$

where l_f and l_0 denote the length of the cell in the x direction in the final and initial configurations, respectively.

In order to assess how edges and surfaces influence the variations of E_{ijk}, we calculate all local variations in E_{ijk} over the cross section. This is done in the following manner. The local stress tensor $\boldsymbol{\sigma}_i$ is calculated for a material point (i.e., atom i),

$$\boldsymbol{\sigma}_i=-\frac{1}{2V_{\alpha,i}}\sum_{j\neq i}\boldsymbol{r}_{ij}\otimes\boldsymbol{f}_{ij}, \tag{16}$$

where $V_{\alpha,i}$ denotes the atomic volume associated with atom i, and the sum of atomic volumes adds up to the total volume

$$\sum_{i}^{n}V_{\alpha,i}=V. \tag{17}$$

For simplicity, in this paper, we assume that the local distortions of the bcc lattice are small and, consequently, that the atomic volumes are equal, i.e.,

$$\sum_{i}^{n}V_{\alpha,i}=nV_{\alpha}=V. \tag{18}$$

Therefore, it is assumed that the atomic volume can be set to $V_{\alpha}=\lambda\kappa\eta a_0^3/2$. Then, the directional Young's modulus associated with atom i can be defined as

$$E_{i,ijk}=\frac{\sigma_{i,xx}^{f}-\sigma_{i,xx}^{0}}{\epsilon_{xx}}, \tag{19}$$

and, consequently,

$$E_{ijk}=\frac{1}{n}\sum_{i}^{n}E_{i,ijk}. \tag{20}$$

The directional Young's modulus for cross sections with $N_{xy}=N_{xz}$ both for relaxed and unrelaxed nanowires of orientation I is given in Fig. 8(a) and for orientations II and III in Fig. 8(b) along with the corresponding ideal values calculated from Eqs. (5) and (6) using the elastic constants from the potential given in Table I.

1. Orientation I

In Fig. 8(a), it is observed that there is a significant decrease in E_{100} with increasing cross-sectional dimensions. The directional Young's modulus can be compared between the largest and the smallest specimens. The largest squared specimen has a cross section corresponding to $N_{xy}=N_{xz}=241$, meaning that it has sides that are approximately 345 Å. The smallest specimen has $N_{xy}=N_{xz}=7$; hence, the sides are of the order of 10 Å. Comparing these two, it is observed that E_{100} for the smallest specimen is about 177.6 GPa and decreases with increasing size to 136.1 GPa for the largest, which is quite close to the bulk value of 135.0 GPa as calculated using Eq. (5). This means that there is a decrease of about 42 GPa between the smallest and the largest specimens, corresponding to a decrease of about 23.4%. The second largest squared specimen, with $N_{xy}=N_{xz}=161$ with sides of the order of 231 Å, has a directional Young's modulus of about 136.8 GPa. Comparing the second largest specimen and the largest, it is noted that the decrease is significantly smaller than as compared between the largest and the smallest and is of the order of 0.74 GPa. This corresponds to a decrease of about 0.5%, which clearly suggests a convergence behavior. Comparing the relaxed and the unrelaxed (i.e., $\lambda_{\mathrm{I}}=1$) curves, it can be observed that the unrelaxed nanowires display a more compliant behavior than the

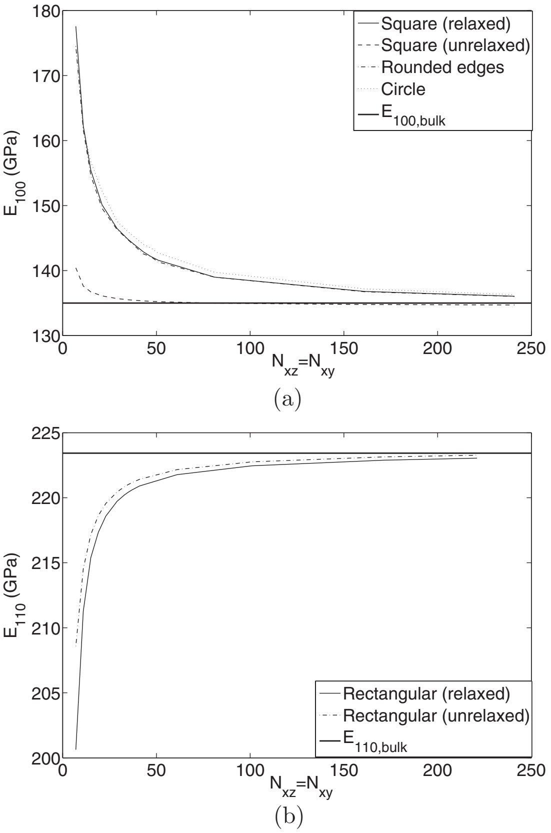

(a)

(b)

FIG. 8. E_{ijk} for nanowires with $N_{xy}=N_{xz}$, calculated using Eq. (20): (a) orientation I along with two types of area reductions and (b) orientations II and III.

relaxed ones. Consequently, this implies that the distortion of the atomic structure that arises due to the surface stresses influence the elastic properties and, for orientation I, the length contraction makes the nanowires stiffer. Furthermore, this also suggests that the elastic behavior is non linear, which is quite common among single crystals.[28,44]

As a result of the reduction of number of neighbors for the atoms near the surfaces and at the edges, we expect these regions to have different elastic properties from the bulk. This is mainly because of the reduced number of interaction atoms and the local distortions that arise in these regions, which result in interactions that are different from those in the bulk. In Figs. 9(a)–9(c), the local directional Young's modulus distributions of two adjacent yz planes for three cross sections with equally many xy as xz planes, i.e., $N_{xy}=N_{xz}$, are seen. In Figs. 9(a)–9(c), we have $N_{xy}=N_{xz}=21$, $N_{xy}=N_{xz}=41$, and $N_{xy}=N_{xz}=241$, respectively, and it is observed that there are bands from the edges toward the center along the $\langle 110 \rangle$ directions, where $E_{i,100}$ exceeds the magnitude of the surrounding atoms. These bands are believed to be artifacts emanating from the distortions that arise close to the edges, cf. Fig. 6(a). It is also noted that, as the bands meet toward the center of the cross section, there is an area of increased stiffness. In Figs. 9(d) and 9(e), the local directional Young's modulus distribution for prestrained nanowires with $N_{xy}=N_{xz}=21$ and $N_{xy}=N_{xz}=41$ can be seen. The overall impression is that they are weaker than the corresponding relaxed nanowires. However, similar types of bands are present. To determine to what extent the geometry induces this variance, we have a rectangular cross section with $N_{xy}=241, N_{xz}=81$ in Fig. 9(f) from which it can be seen that these effects seem to remain as the bands intersect but are geometrically limited so that toward the bulk or core at the center of the cross section, and only minor variations are present. Hence, the edge influences are neglectable at the center, away from the edges when the width is significant compared to the height.

Dividing the cross section into subregions, similar to previous investigators,[20,25] allows one to study how they behave separately. To this end, for this orientation, the cross section has been divided into three sections, surface, edge, and core. The subdivision has taken place as schematically illustrated by the inset of Fig. 10(b), where the outermost atom planes around the entire cross section are regarded as surfaces. The edge atoms consist of the 32 atoms that are situated inside the four squares as illustrated in Fig. 10(b), and the rest constitute the core atoms. In Fig. 10(a), the directional Young's modulus can be seen for the different subregions, and in Fig. 10(b), the fractions of the total number of atoms are shown. For both the relaxed and unrelaxed nanowires, E_{100} decreases with increasing size for all the regions and, similar to in Fig. 8(a), the unrelaxed nanowires show a high degree of convergence. Not very surprisingly, the different regions converge toward different values but, because of the great fraction of core atoms, the core regions of both the relaxed and the unrelaxed nanowires converge toward the ideal bulk value. As another observation it can be seen that, in accordance with Fig. 9(c), for large sizes, the edges are the stiffest and the surfaces are the weakest, but for small samples, all regions display quite similar elastic properties. Consequently, for small samples, the regional fractions are quite unimportant, and it is mostly the elastic properties that dictate the behavior.

When considering the regions away from the edges, we can see that there are different elastic behaviors for different sizes. Figures 11(a) and 11(b) display the local variations in $E_{i,100}$ along the z coordinate normalized by the width b of relaxed and unrelaxed nanowires, respectively, for different cross section sizes. Regarding the relaxed nanowires, cf. Fig. 11(a), it can be seen that the behavior appears to be quite different in the two limits of small and large samples. It can be observed that for the four smallest specimens, $7 \leqslant N_{xy} = N_{xz} \leqslant 21$, there is a local maximum at the outermost atom plane, followed by a local minimum at the second atom plane. Thereafter, they display monotonous stiffening and reach a maximum at the center of the specimen. The largest specimens, $81 \leqslant N_{xy} = N_{xz} \leqslant 241$, display a different behavior than the aforementioned. The outermost atom plane is the weakest, followed by a stiffening between the first and third atom planes, where a local maximum is obtained. Thereafter, weakening occurs for the two subsequent atom planes and a local minimum is observed at the fifth atom plane from the surface, followed by small local fluctuations and a maximum at the center of the specimen. The intermediate specimens have a behavior which can be described as a transition between the smaller and the larger specimen behaviors. For the specimen with $N_{xy}=N_{xz}=29$, it is noted that there is a local maximum at the outermost surface and a local minimum at

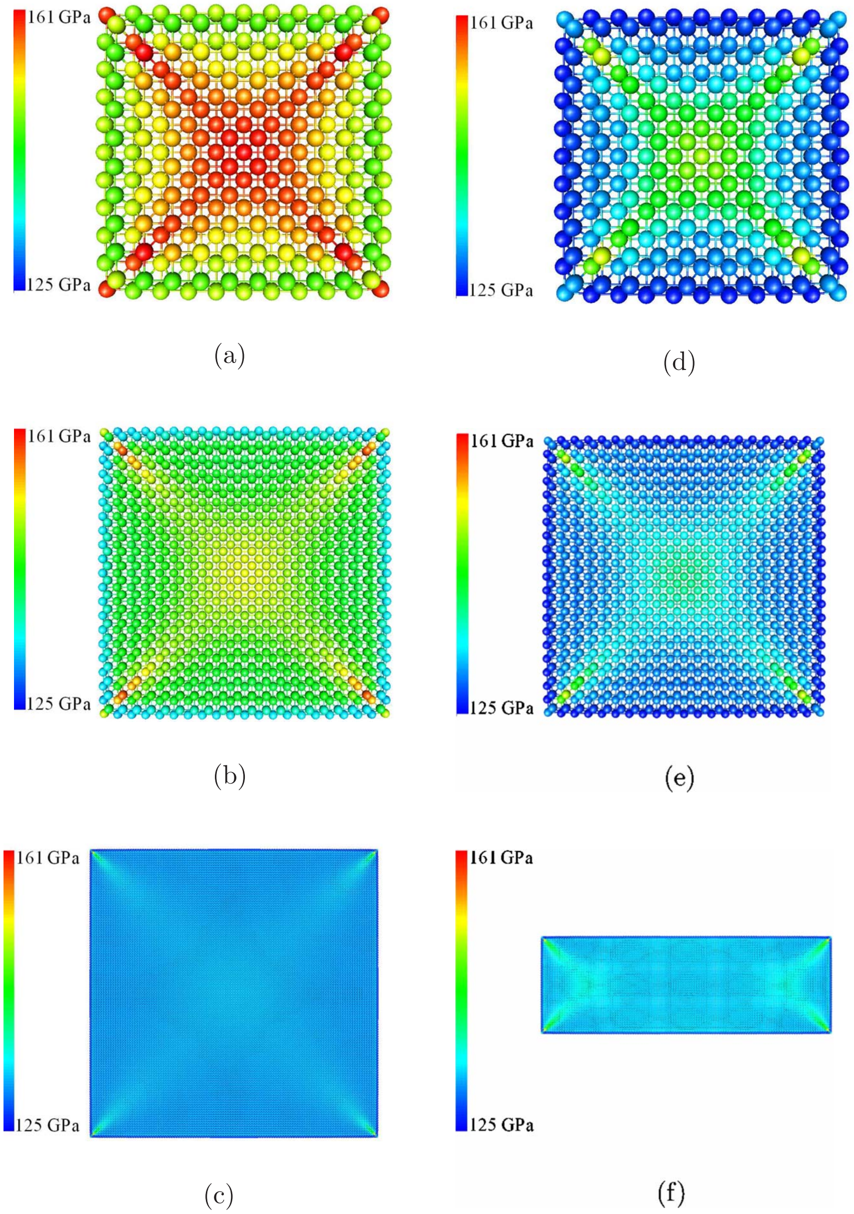

(a) (d)

(b) (e)

(c) (f)

FIG. 9. (Color online) Local directional Young's modulus $E_{i,100}$ distribution of orientation I: (a) $N_{xy}=N_{xz}=21$, (b) $N_{xy}=N_{xz}=41$, (c) $N_{xy}=N_{xz}=241$, (d) $N_{xy}=N_{xz}=21$ (unrelaxed), (e) $N_{xy}=N_{xz}=41$ (unrelaxed), and (f) $N_{xy}=241$, $N_{xz}=81$ [the atomistic figures are generated with GOPENMOL (Ref. 45)].

the second atom plane. This is followed by stiffening and a local maximum at the fourth atom plane from the surface; thereafter, a local minimum is observed at the fifth atom plane, followed by monotonous stiffening and a maximum at the center of the cross section. For the specimens in the interval $35 \leqslant N_{xy}=N_{xz} \leqslant 51$, a local minimum is found at the outermost atom plane, which is followed by stiffening until the fourth atom plane where a local maximum is found. Thereafter, weakening occurs between the fourth and the fifth atom plane, followed by monotonous stiffening, with a maximum in the center of the cross section. The unrelaxed nanowires, cf. Fig. 11(b), display a more unified behavior. The surfaces appear to have similar elastic properties, and the significant differences in $E_{i,100}$ between the relaxed and the prestrained specimens for the smaller sized nanowires also indicate that the elastic behavior is nonlinear.

In order to study the geometric influence on the elastic properties of orientation I, in addition to the previous simulations, two types of reduced cross sections have been studied. First, a circular cross section with a radius that equals half the width of the corresponding square cross section and, second, the sharp edges are rounded in such a manner that every atom that lies outside 80% of the distance between the center and the edges of the corresponding square cross section are removed. In Figs. 12(a) and 12(b), the local directional Young's moduli for two circular cross sections are given with $N_{xy}=N_{xz}=43$ and $N_{xy}=N_{xz}=241$, respectively. For the smaller of the two, it can be observed that there are bands present whenever there are steps in the surface, and the bands are going along the $\langle 110 \rangle$ directions from the steps.

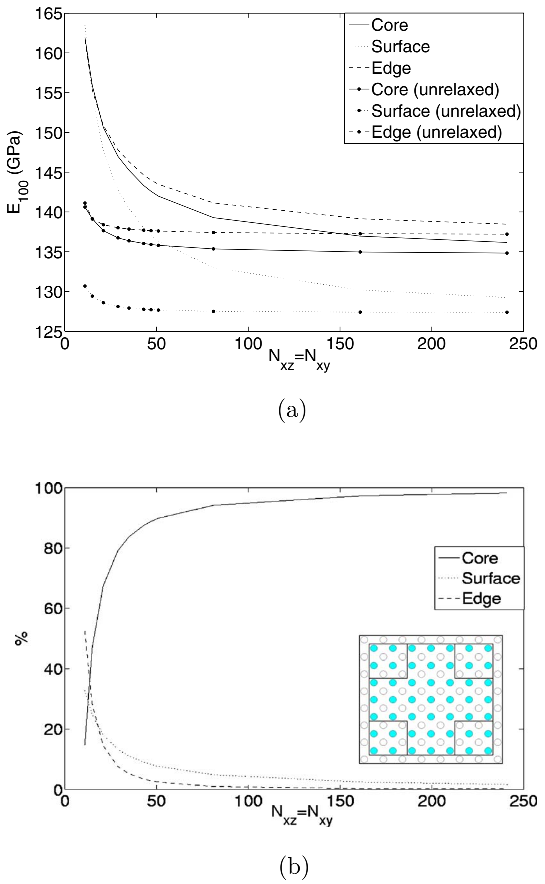

FIG. 10. (Color online) (a) Directional Young's modulus E_{100} for the different subregions of orientation I both for relaxed and unrelaxed nanowires and (b) the fractions of atoms belonging to the different subregions (the inset schematically displays the cross-sectional subdivision).

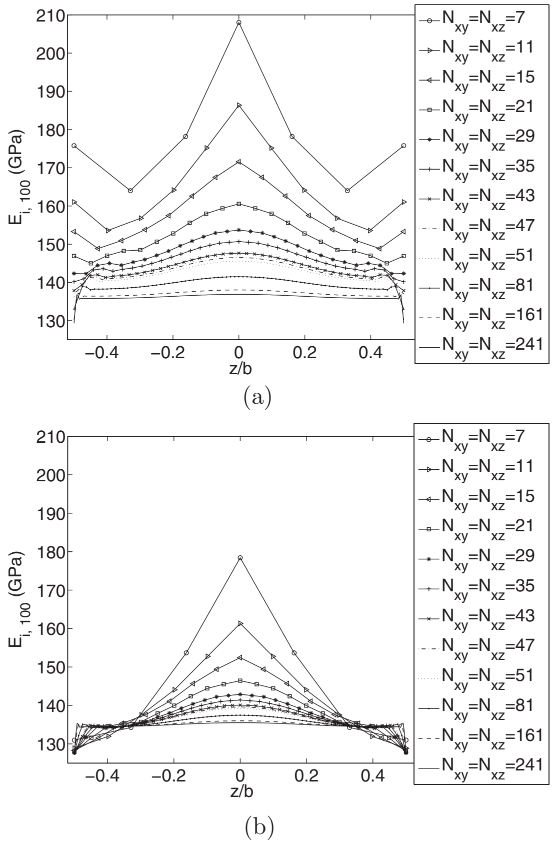

FIG. 11. Variations in $E_{i,100}$ along the z axis through the center of mass of orientation I for (a) relaxed and (b) unrelaxed nanowires.

Similar trends can be observed for the larger one, since there are deviations near the surfaces originating from surface steps. However, the overall impression is that these deviations are rather short ranged, and this specimen displays a more homogeneous distribution than the smaller specimen. In Figs. 12(c) and 12(d), the edges have been rounded only. Similar to the aforementioned, these cross sections also display bands near surface steps, but they are more clearly distinguishable than for the circular cross section. In Fig. 8(a), the directional Young's moduli of the reduced cross sections, along with the square cross sections and the ideal value, are illustrated. It can be observed that, on average, there are only minor deviations between the square cross sections and the reduced ones.

2. Orientations II and III

From Figs. 3(b) and 3(c), it can be realized that orientations II and III are the same, except for a 90° rotation around the x axis and, consequently, for these simulations they will yield the same results. From Fig. 8(b), it is observed that E_{110} has significantly different characteristics than E_{110}. As a first observation, it can be noted that E_{110} increases with increasing cross-sectional dimensions. The largest sample has $N_{xy}=N_{xz}=221$, which corresponds to sides of the orders of 317 and 448 Å, and the directional Young's moduli for these samples are found to be 223.0 GPa, which is quite close to the bulk value of 223.4 GPa calculated using Eq. (6). This can be compared with the smallest with $N_{xy}=N_{xz}=7$, with sides of about 10 and 14 Å, with the directional Young's modulus of 200.6 GPa. This corresponds to an increase of about 11%. The second largest sample has $N_{xy}=N_{xz}=171$, and the sides are 245 and 347 Å. The directional Young's modulus for this sample is found to be 222.9 GPa, which means that the increase between the second largest and the largest specimens is of the order of 0.04%. This suggests a clear tendency of convergence. Moreover, it can be noted that the prestrained specimens are stiffer than the completely relaxed specimens, which also implies that there is a nonlinear elastic behavior.

In Figs. 13(a)–13(c), the local directional Young's modulus distributions of two adjacent yz planes for three cross sections with equally many xy as xz planes, i.e., $N_{xy}=N_{xz}$, are given. Similar to for orientation I, there are bands from the edges in the directions 45° from the surfaces and, hence, we can conclude that these are merely geometrical artifacts as a consequence of the sharp edges. They are, however, not as long ranged as for orientation I but mainly confined close to the edges. It should also be noted that the different surfaces have different elastic properties. For instance, in Fig. 13(c), it can be seen that the directional Young's modulus, far away from the edges, is around 150 GPa for a {100} surface in a

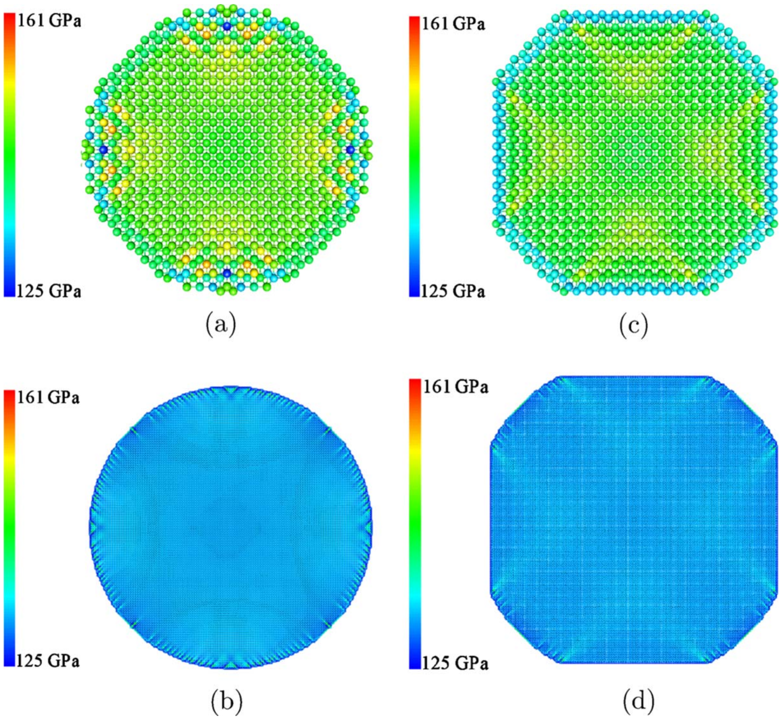

FIG. 12. (Color online) Local directional Young's modulus $E_{i,100}$ for reduced cross sections [circular: (a) $N_{xy}=N_{xz}=43$ and (b) $N_{xy}=N_{xz}=241$; rounded edges: (c) $N_{xy}=N_{xz}=43$ and (d) $N_{xy}=N_{xz}=241$].

$\langle 011\rangle$ direction, whereas for a $\{01\bar{1}\}$ surface in the $\langle 011\rangle$ direction, it is found to be approximately 190 GPa. Another observation, though not very surprising, can be made by comparing a $\{100\}$ surface in a $\langle 011\rangle$ direction with the same type of surface in the $\langle 100\rangle$ direction. This can be observed in Fig. 11(a), showing the directional Young's modulus of about 130 GPa. Consequently, we can draw the conclusion that surfaces have different elastic properties in different directions. Furthermore, it can be seen that the surfaces are significantly weaker than the bulk, and that there is a large

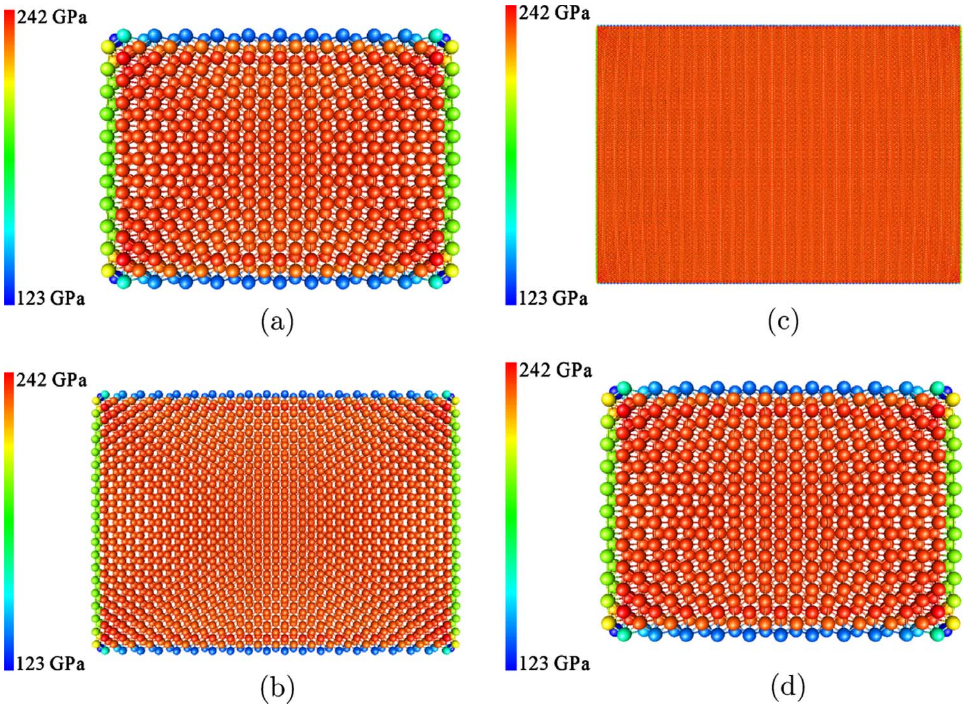

FIG. 13. (Color online) Local directional Young's modulus $E_{i,110}$ distribution of orientations II and III: (a) $N_{xy}=N_{xz}=23$, (b) $N_{xy}=N_{xz}=41$, (c) $N_{xy}=N_{xz}=221$, and (d) $N_{xy}=N_{xz}=23$ (unrelaxed).

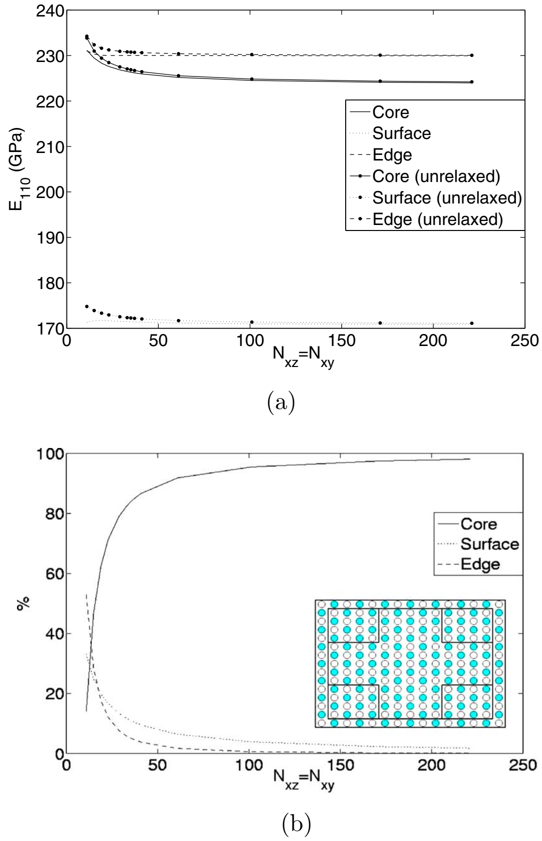

(a)

(b)

FIG. 14. (Color online) (a) Directional Young's modulus E_{110} for the different subregions of orientations II and III both for relaxed and unrelaxed nanowires and (b) the fractions of atoms belonging to the different subregions (the inset schematically displays the cross-sectional subdivision).

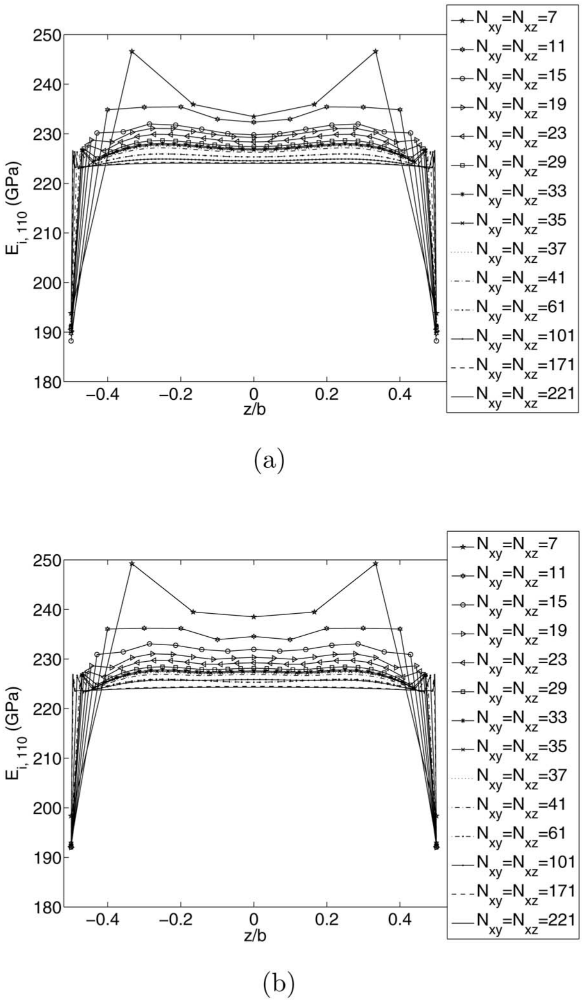

(a)

(b)

FIG. 15. Variations in $E_{i,110}$ along the z axis through the center of mass of orientation II for (a) relaxed and (b) unrelaxed nanowires.

difference in $E_{i,110}$ between the outermost atom planes as compared to its neighboring plane. In Fig. 13(d), the local directional Young's modulus distribution for a prestrained nanowire with $N_{xy}=N_{xz}=23$ is displayed as compared to the corresponding relaxed nanowire, cf. Fig. 13(a), and there are only minor differences present.

Similar to what was done for orientation I, the cross section is divided into three regions as illustrated by the inset of Fig. 14(b). The surface atoms consist of the outermost atoms around the cross section, and the edge atoms are the 64 atoms confined in the rectangular regions as can be seen in Fig. 14(b), whereas the rest constitute the core atoms. The directional Young's modulus for the different regions can be seen in Fig. 14(a) both for relaxed and unrelaxed nanowires. As can be noted, all the regions display a weakening with increasing size except for the unrelaxed surface region. The decrease is, however, rather small for all regions and not to the extent as was seen for orientation I. Moreover, it is observed that the relaxed and prestrained regions have quite similar elastic properties and that there is a large gap in magnitude between the surface region and the other ones. The surfaces are always softer than the core, whereas the edge regions are stiffer. Consequently, it is mostly the fractions of the regional atoms that dictate the elastic behavior for this orientation, as the edges and surfaces dominate for the smaller nanowires and the since surfaces are being more compliant, it is natural for the smaller nanowires to be weaker. This is in opposition to the larger nanowires where the core atoms are dominating and, consequently, the global directional Young's modulus converges to that of the core.

The variations in $E_{i,110}$ along the z axis through the center of mass for orientation II can be seen in Figs. 15(a) and 15(b) for relaxed and unrelaxed specimens, respectively. It can be observed, in accordance with Figs. 13(a)–13(c), that the outermost plane is considerably much weaker than the adjacent plane. Moreover, for the completely relaxed specimens, it is observed for the smallest specimen, $N_{xy}=N_{xz}=7$, that there is a significant local maximum at the second atom plane. A maximum is also observed at the second atom plane for the larger specimens, $N_{xy}=N_{xz}\geqslant 19$, but not for $N_{xy}=N_{xz}=11$ and $N_{xy}=N_{xz}=15$ where the local maximum is found at the fourth atom plane from the surface, followed by a decrease and a local minimum at the center. The larger specimens have two local maxima and three local minima, where the first maximum is located at the second atom plane from the surface and the second is situated around at where the bands of in-

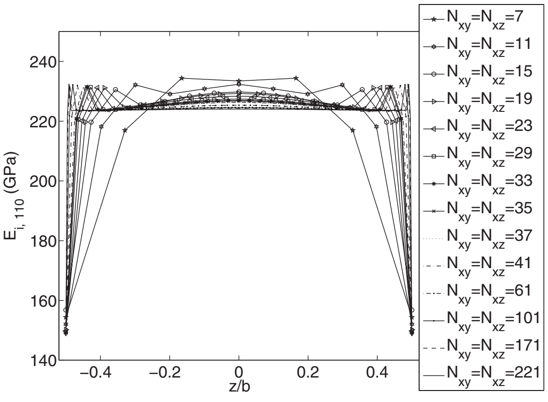

(a)

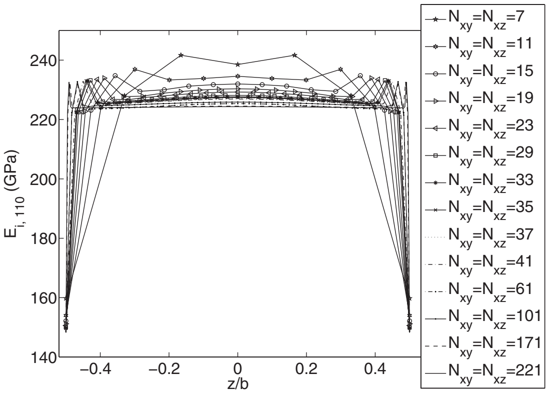

(b)

FIG. 16. Variations in $E_{i,110}$ along the z axis through the center of mass of orientation III for (a) relaxed and (b) unrelaxed nanowires.

creased directional Young's modulus emanating from the edges intersect. The minima are situated at the outermost atom plane, between the second atom plane and the second maximum, and the last minimum is situated at the center. Comparing the relaxed and prestrained nanowires, there is a slight difference in the elastic properties. As can be seen from Figs. 15(a) and 15(b), the prestrained samples appear to be somewhat stiffer. However, the overall impression is that they are quite similar.

Regarding orientation III, cf. Figs. 16(a) and 16(b), the overall behavior is similar to that of orientation II except for a few differences. The outermost atom plane is the weakest plane for all the specimens and the third from the surface is always the stiffest. All the specimens experience a local minimum between the third plane and the center, where there is a local maximum, except for the smallest specimen, $N_{xy}=N_{xz}=7$, which has a local minimum at the center.

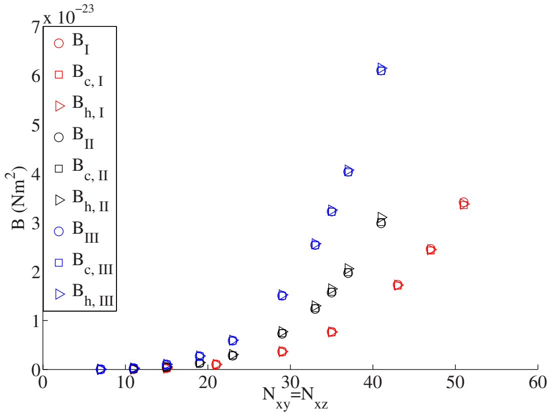

FIG. 17. (Color online) The bending stiffness for the different orientations for $N_{xy}=N_{xz}$ [circles, Eq. (23); squares, Eq. (24); triangles, Eq. (25)].

C. Bending simulations

From Eq. (8), the bending stiffness B from the results of the bending simulations can be estimated. Considering that the four yz planes at the clamped end are fixed, the length L of the beam is approximated as

$$L=(N_{yz}-4)\lambda d_x, \tag{21}$$

where N_{yz} is the number of yz planes and d_x is the interplanar distance between two adjacent yz planes. The quantity γ is calculated using the fact that the load is distributed over the six outermost yz planes leading to

$$\gamma=\frac{N_{yz}-10}{N_{yz}-4}. \tag{22}$$

The interplanar distance d_x depends on the crystallographic orientation of the beam, i.e., $d_x=a_0/2$ for orientation I and $d_x=a_0/\sqrt{2}$ for orientations II and III. Thus, from Eqs. (8), (21), and (22), we get

$$B=\frac{q(N_{yz}-4)^3 d_x^3\lambda^3}{24\delta}\left[3+3\left(\frac{N_{yz}-10}{N_{yz}-4}\right)+3\left(\frac{N_{yz}-10}{N_{yz}-4}\right)^2-\left(\frac{N_{yz}-10}{N_{yz}-4}\right)^3\right], \tag{23}$$

where all the parameters on the right hand side are obtained from the simulations, and hence it is possible to calculate $B=B(N_{xy},N_{xz})$. In order for the assumption of slenderness to be satisfied, all the beams were constructed so that $10.6<N_{yz}d_x/(N_{xz}d_y)<40.4$ is satisfied.

Furthermore, we can approximate the bending stiffness as a composite beam,

$$B_c=\sum_i^{N_c} E_{i,ijk}y_i^2\Delta A, \tag{24}$$

from the local distribution [Eq. (14)] and as a homogeneous beam with averaged directional Young's modulus [Eq. (20)],

$$B_h=E_{ijk}I=E_{ijk}\sum_i^{N_c} y_i^2\Delta A, \tag{25}$$

where the summation i is over all the atoms in two adjacent yz planes, $\Delta A=a_0^2\kappa\eta/2$ for orientation I and $\Delta A=a_0^2\kappa\eta/(2\sqrt{2})$ for orientations II and III.

A comparison between the three different expressions [Eqs. (23)–(25)] is given in Fig. 17, where it can be seen that there is a consistency between the different approaches. The maximum deviations are 5.3%, 12.8%, and 3.9%, for orientations I, II, and III, respectively, and are found for the small-

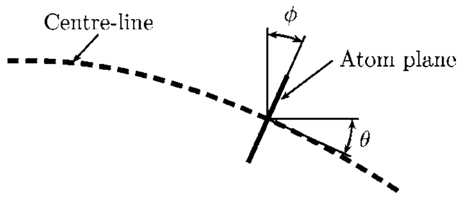

FIG. 18. Schematic construction of the angles ϕ and θ.

est specimens. In order to check the validity of Bernoulli's beam theory in these applications, we define two angles, ϕ and θ, that are the angle between the x axis and the centerline and the angle between the y axis and an yz plane in the deformed configuration, respectively, cf. Fig. 18. These two angles have to be equal in order for the cross section to be perpendicular to the centerline. The angles ϕ and θ for some of the different bending simulations can be seen in Figs. 19(a)–19(c) where it can be observed that there is a consistent behavior between ϕ and θ with only minor variations. Hence, it can be concluded that there is only little shearing present, and, consequently, Bernoulli's beam theory is valid for the simulations.

VI. CONCLUSIONS

In this paper, an analysis of the elastic behavior of nanowires and nanobeams of bcc iron through MS tensile and bending simulations is presented. From the tensile simulations, it is observed that there is a strong size dependence in the directional Young's modulus. For all the different crystallographic orientations, there is, however, a clear tendency of convergence for the larger specimens toward corresponding bulk values. The size dependence is a consequence of the surfaces' and edges' deviating elastic properties, which both can be stiffer or more compliant than the bulk. Consequently, these contributions play a significant role for smaller specimens. Different crystallographic orientations display completely different behaviors since the directional Young's modulus of orientation I increases with decreasing cross-section size, whereas orientations II and III display the opposite tendency, i.e., decreases with decreasing cross section size, cf. Figs. 5 and 6. Dividing the cross section in subregions (edges, surfaces, and core) reveals that the edges are stiffer than the core, whereas surfaces are more compliant. Moreover, from the subdivision, it can be observed that for orientation I, all the regions display significant stiffening with decreasing size, and in the limit of small samples, all the regions display quite similar elastic properties. However, they converge toward different values in the limit of large samples, where the core regions converge toward the ideal bulk value. For orientations II and III, the different regions also display stiffening with decreasing size. However, the stiffening is not of the same extent as for orientation I, and there is a significant difference in magnitude between the surfaces and the edge and core regions. Consequently, for orientations II and III, the small samples are weaker due to the large fraction of surface atoms. For orientation I, the regional fractions do not dictate the elastic properties for small samples to that extent because of the similar elastic properties of the regions. However, it is rather the significant weakening of all the regions with increasing size that explains the elastic behavior. Comparing the completely relaxed and the prestrained nanowires, it is evident that the length contraction that arises in order to balance the surface stresses distorts the lattice and, consequently, influences the elastic properties. This implies that the elastic behavior is not entirely linear. It should, however, be noted that this effect is quite small for orientations II and III.

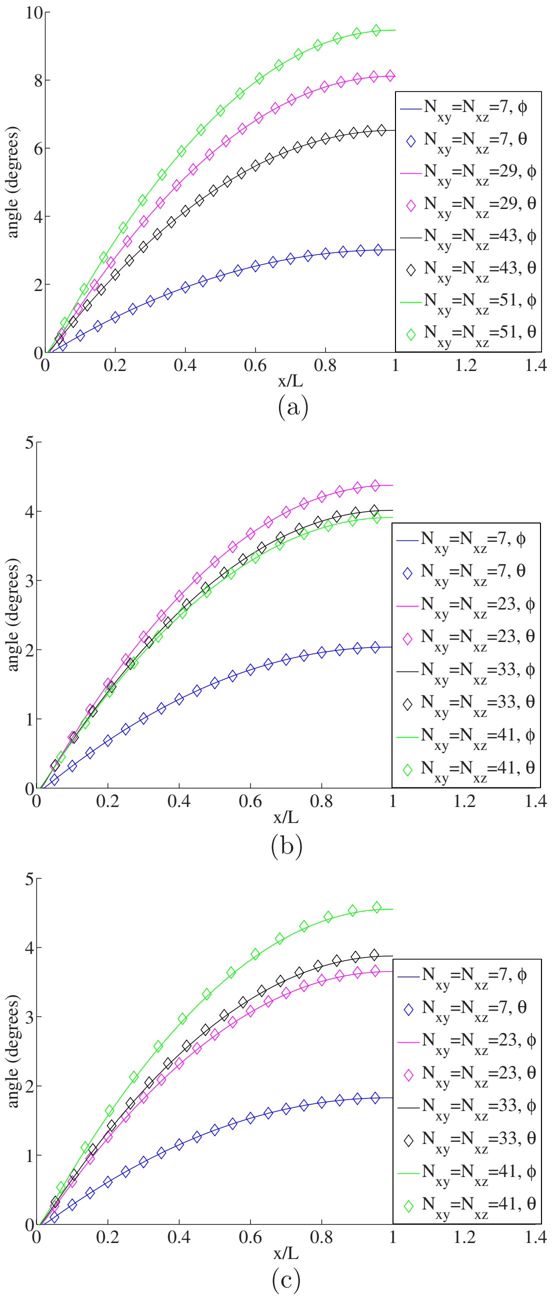

FIG. 19. (Color online) Angles ϕ and θ for $N_{xy}=N_{xz}$ for (a) for orientation I, (b) orientation II, and (c) orientation III.

Studying the cross sections after relaxation reveals that for orientation I, the outermost {100} surfaces displace themselves away from the center as the edges are displaced toward the center, giving the otherwise square cross section a more rounded shape, distorting the regions around the edges.

For orientation II, the {110} surfaces move toward the center of the cross section. It has also been observed that steps in the surfaces give rise to deviations from the perfect cubic lattice, contributing to local deviations in the directional Young's modulus inducing deviating bands in the cross section, leading to a heterogeneous or composite-structure-like behavior, which can influence the bending stiffness. Reducing the cross sections by rounding the edges, or giving the cross section a more circular shape, has little influence on the average directional Young's modulus, but it does, nevertheless, influence the local distribution. For orientation I, it was observed that, after edge rounding, there were still highly distinguishable bands that were originating at the intersections between the straight surface parts and the rounding. There were also bands of deviations, significantly more short ranged, emanating from the surface roughness arising due to the discrete nature of atomic crystal arrangements.

The bending stiffness was calculated in three different ways: through bending simulations, through integration over the cross section using the local distribution of the directional Young's modulus obtained from the tensile simulations, and by using the average directional Young's modulus. The three different approaches displayed a consistent behavior, with only minor deviations. Furthermore, the simulations also show that the shearing is minimal and, therefore, Bernoulli's beam theory is a valid approximation for the simulations.

ACKNOWLEDGMENTS

This work has been supported by the Swedish Research Council. The simulations were performed using the computational resources at LUNARC, Center for Scientific and Technical Computing, Lund University. The authors gratefully thank G. Karlström, B. Jönsson, A. Machová, A. Hartmaier, and P. Lidström for helpful discussions.

---

*par.olsson@mek.lth.se

[1] A. Gupta, D. Akin, and R. Bashir, Appl. Phys. Lett. **84**, 1976 (2004).

[2] M. B. Viani, T. E. Schäffer, A. Chand, M. Reif, H. E. Gaub, and P. K. Hansma, J. Appl. Phys. **86**, 2258 (1999).

[3] B. Ilic, D. Czaplewski, H. G. Craighead, P. Neuzil, C. Campagnolo, and C. Batt, Appl. Phys. Lett. **77**, 450 (2000).

[4] T. D. Stowe, K. Yasumura, T. W. Kenny, D. Botkin, K. Wago, and D. Rugar, Appl. Phys. Lett. **71**, 288 (1997).

[5] D. J. Sellmyer, M. Zheng, and R. Skomski, J. Phys.: Condens. Matter **13**, R433 (2001); J. B. Wang, X. Z. Zhou, Q. F. Liu, D. S. Xue, F. S. Li, B. Li, H. P. Kunkel, and G. Williams, Nanotechnology **15**, 485 (2004); X. Y. Zhang, G. H. Wen, Y. F. Chan, R. K. Zheng, X. X. Zhang, and N. Wang, Appl. Phys. Lett. **83**, 3341 (2003).

[6] Y. L. Sun, Y. Dai, L. Q. Zhou, and W. Chen, Solid State Phenom. **121-123**, 17 (2007).

[7] A. Hultgren, M. Tanase, C. S. Chen, G. J. Meyer, and D. H. Reich, J. Appl. Phys. **93**, 7554 (2003).

[8] E. W. Wong, P. E. Sheehan, and C. M. Lieber, Science **227**, 1971 (1997).

[9] H. G. Craighead, Science **290**, 1532 (2000).

[10] S. G. Nilsson, E. L. Sarwe, and L. Montelius, Appl. Phys. Lett. **83**, 990 (2003); S. G. Nilsson, X. Borrisé, and L. Montelius, *ibid.* **85**, 3555 (2004).

[11] S. Sundararajan and B. Bhushan, Sens. Actuators, A **101**, 338 (2002).

[12] S. Cuenot, S. Demoustier-Champagne, and B. Nysten, Phys. Rev. Lett. **85**, 1690 (2000).

[13] S. Cuenot, C. Frétigny, S. Demoustier-Champagne, and B. Nysten, J. Appl. Phys. **93**, 5650 (2003).

[14] S. Cuenot, C. Frétigny, S. Demoustier-Champagne, and B. Nysten, Phys. Rev. B **69**, 165410 (2004).

[15] X. Li, T. Ono, Y. Wang, and M. Esashi, Appl. Phys. Lett. **83**, 3081 (2003).

[16] C. Y. Nam, P. Jaroenapibal, D. Tham, D. E. Luzzi, S. Evoy, and J. E. Fischer, Nano Lett. **6**, 153 (2006).

[17] E. A. Ivanova, A. M. Krivtsov, and N. F. Morozov, Dokl. Akad. Nauk **385**, 494 (2002) [Dokl. Phys. **47**, 620 (2002)]; Fatigue Fract. Eng. Mater. Struct. **26**, 715 (2003).

[18] A. M. Krivtsov and N. F. Morozov, Fiz. Tverd. Tela (Leningrad) **44**, 2158 (2002) [Sov. Phys. Solid State **44**, 2260 (2002)]; Dokl. Akad. Nauk **381**, 825 (2001) [Dokl. Phys. **46**, 825 (2001)].

[19] O. S. Loboda and A. M. Krivtsov, Mekh. Tverd. Tela **4**, 27 (2005) [Mech. Solids **40**, 20 (2005)].

[20] J. Q. Broughton, C. A. Meli, P. Vashishta, and R. K. Kalia, Phys. Rev. B **56**, 611 (1997).

[21] P. Heino, H. Häkkinen, and K. Kaski, Europhys. Lett. **41**, 273 (1998).

[22] P. Villain, P. Beauchamp, K. F. Badawi, P. Goudeau, and P.-O. Renault, Scr. Mater. **50**, 1247 (2004).

[23] Y.-H. Wen, Z.-Z. Zhu, G.-F. Shao, and R.-Z. Zhu, Physica E (Amsterdam) **27**, 113 (2005).

[24] H. S. Park and J. A. Zimmerman, Phys. Rev. B **72**, 054106 (2005).

[25] J. Diao, K. Gall, and M. L. Dunn, J. Mech. Phys. Solids **52**, 1935 (2004).

[26] F. H. Streitz, K. Sieradzki, and R. C. Cammarata, Phys. Rev. B **41**, 12285(R) (1990).

[27] L. G. Zhou and H. Huang, Appl. Phys. Lett. **84**, 1940 (2004).

[28] H. Liang, M. Upmanyu, and H. Huang, Phys. Rev. B **71**, 241403(R) (2005).

[29] H. A. Wu, Mech. Res. Commun. **33**, 9 (2006); Eur. J. Mech. A/Solids **25**, 370 (2006).

[30] H. A. Wu, Comput. Mater. Sci. **31**, 287 (2004).

[31] H. He and N. J. Tao, in *Encyclopedia of Nanoscience and Nanotechnology*, edited by H. S. Nalwa (American Scientific, Valencia, CA, 2004).

[32] M. A. Meyers and K. K. Chawla, *Mechanical Behavior of Materials* (Prentice-Hall, Upper Saddle River, NJ, 1999).

[33] L. D. Landau and E. M. Lifshitz, *Theory of Elasticity* (Pergamon, London, 1959).

[34] E. Bitzek, P. Koskinen, F. Gähler, M. Moseler, and P. Gumbsch, Phys. Rev. Lett. **97**, 170201 (2006).

[35] M. P. Allen and D. J. Tildesley, *Computer Simulation of Liquids* (Clarendon, Oxford, 1987).

[36] H. J. C. Berendsen, J. P. M. Postma, W. F. van Gunsteren, A. DiNola, and J. R. Haak, J. Chem. Phys. **81**, 3684 (1984).

[37] J. H. A. Hagelaar, E. Bitzek, C. F. J. Flipse, and P. Gumbsch, Phys. Rev. B **73**, 045425 (2006).

[38] M. W. Finnis and J. E. Sinclair, Philos. Mag. A **50**, 45 (1984); **53**, 161(E) (1986).

[39] A. Machová and G. J. Ackland, Modell. Simul. Mater. Sci. Eng. **6**, 521 (1998).

[40] J. A. Rayne and B. S. Chandrasekhar, Phys. Rev. **122**, 1714 (1961).

[41] D. C. Rapaport, *The Art of Molecular Dynamics Simulation*, 2nd ed. (Cambridge University Press, Cambridge, 1995).

[42] D. Frenkel and B. Smit, *Understanding Molecular Simulation: From Algorithms to Applications*, 2nd ed. (Academic, San Diego, 1996).

[43] M. Zhou, Proc. R. Soc. London, Ser. A **459**, 2347 (2003).

[44] G. W. Sears, A. Gatti, and R. L. Fullman, Acta Metall. **2**, 727 (1954); S. S. Brenner, J. Appl. Phys. **27**, 1484 (1956).

[45] L. Laaksonen, J. Mol. Graphics **10**, 33 (1992); D. L. Bergman, L. Laaksonen, and A. Laaksonen, J. Mol. Graphics Modell. **15**, 301 (1997).